J Eng Math (2010) 66:293–310
DOI 10.1007/s10665-009-9340-9

Ultrasound detection of externally induced microthrombi cloud formation: a theoretical study

G. T. Guria · M. A. Herrero · K. E. Zlobina

Received: 1 December 2008 / Accepted: 23 September 2009 / Published online: 14 October 2009

Abstract A mathematical model for the formation of microaggregates (microthrombi) of fibrin polymers in blood flow is considered. It is assumed that the former are induced by an external source (which may be of inflammatory or tumor nature) located in a tissue near the vessel. In either case, specific agents (e.g. cytokines) are emitted from that pathological site. Such substances permeate through the vessel wall to act as primary activators of blood coagulation. A mathematical criterion to describe the formation of an intravascular microthrombi cloud, which is interpreted as an early indicator of subsequent macroscopic thrombi formation is discussed. Such criteria are compared with available experimental detection tests for microthrombi cloud formation by means of ultrasound techniques. Moreover, a similarity-type relation is proposed that links the location of the unfolding microthrombi cloud and the place at which such primary activator reaches the vessel wall.

Keywords Coagulation equations · Numerical simulation · Similarity laws · Thrombi formation

1 Introduction

"Blood is a juice of very special kind".[1] Human blood is normally in a liquid state, which allows it to carry out its main function: mass transport. However, under suitable conditions blood may experience strong polymerization processes. As a matter of fact, its ability to undergo a localized, rapid phase transition to eventually produce elastic,

[1] Blut ist ein ganz besonderer Saft [1, Part I].

G. T. Guria · K. E. Zlobina (✉)
National Research Center for Haematology, 125167 Moscow, Russia
e-mail: ksen@blood.ru

G. T. Guria
e-mail: guria@blood.ru

G. T. Guria
Moscow Institute of Physics and Technology, 141700 Dolgoprudny, Russia

M. A. Herrero
IMI, Departamento de Matematica Aplicada, Facultad de Matematicas, Universidad Complutense, 28040 Madrid, Spain
e-mail: Miguel_Herrero@mat.ucm.es

gel-like masses or thrombi is essential for survival. In this manner blood loss is quickly stopped in case of small vessel injuries. This phase transition is controlled by a finely tuned set of biochemical reactions known as the blood coagulation cascade [2–4], whose basic ingredients are well established nowadays (see Sect. 2 below).

The resulting product of the aforementioned cascade is thrombin, a key agent in the coagulation process. Under the catalyzing action of thrombin, fibrin monomers are formed from inactive fibrinogen molecules that are always present in blood at basal concentrations. Fibrin monomers then aggregate to form fibrin polymers, which in turn provide a net that keeps inside a number of elements (as for instance platelets) which eventually give rise to solid macroscopic objects known as thrombi. Several mathematical models have been developed to describe the kinetics of thrombin generation [5–10], and the onset of the coagulation process that results in fibrin polymer production [11,12]. On the other hand, early stages of fibrin polymerization, which may subsequently lead to fully developed thrombi, can be acoustically detected in vivo [13,14] and in vitro [15,16] by means of ultrasound (US) devices. Indeed, US imaging is known to display the so-called snowstorm patterns [16]. The latter represent microthrombi clouds, in which any particular element has not yet reached a macroscopic size. Actually, it may well happen that such a cloud is eventually disposed of by blood regulatory mechanisms, but in many cases its presence is known to signal the onset of serious blood disorders [14,17,18]. As a matter of fact, the aim of developing novel diagnostic methods to detect intravascular clot generation provides a motivation for the theoretical investigation to be presented below.

More precisely, the main purpose of this work is to formulate and discuss a mathematical model for the early stages of externally induced thrombi formation in blood flow. It is well known that blood coagulation in vivo may be triggered by pathological processes that take place in nearby tissues [18–21]. As a matter of fact, a critical health condition, known as Disseminated Intravascular Coagulation (DIC), which represents a major contribution to cancer-induced mortality, can be placed in this setting [22,23]. In the model to be discussed below, we assume coagulation to be triggered by substances (e.g. cytokines) being produced at a tissue source, that permeate to the blood through the vessel wall. We shall investigate the relation between the propagation properties of these activating substances and the extent of the induced intravascular coagulation processes. This will be done by means of numerical simulations on a mathematical model, whose relation with the experimental detection techniques mentioned above will be discussed in some detail. In particular, a power-law, similarity-like relation will be proposed for the dependence between the location of an intravascular microthrombi cloud and that of an inducing tissue pathogen source.

We conclude this Introduction by describing the plan of this paper. A key aspect of our approach consists in characterizing the onset of a microthrombi cloud as an early nucleation stage of a sol–gel phase transition [11,12], [24, Chaps. 2 and 7] in a fluid containing polymerizing monomers. Bearing this in mind, in Sect. 2 we introduce our basic activation-polymerization system. In a previous work we have developed a homogeneous, space-independent model of blood coagulation that takes into account both thrombin generation and fibrin polymerization [12]. We now extend that model to a spatially distributed case. In particular, we consider blood coagulation in a vessel under convective and diffusive mass transfer. We then describe in Sect. 3 how ultrasound (US) detection of microthrombi formation can be modeled in mathematical terms. When doing so, we identify some useful functions related to the polymerization process that can be associated to, and determined from, ultrasound devices.

In Sect. 4 we show how the model described in Sect. 2 can be used, in some cases, to track in a vessel a microthrombi cloud which is generated by a source located in nearby tissue. To this end, we shall limit ourselves to consideration of a system in two space dimensions, which describes transversal profiles of blood flow in a suitable vessel subject to a convective velocity. We proceed further by deducing from that system a simplified model which is amenable to efficient numerical simulation, while at the same time retaining key aspects of the process that need to be accounted for. Moreover, the variables appearing in that simplified model are of paramount importance in experimental thrombi detection by ultrasound (US) techniques, as observed in our previous Sect. 3. A number of simulations are presented and discussed, which in particular suggest a similarity-type relation between suitable variables that represent the location of an unfolding microthrombi cloud, and that of an external activator source that triggers such process. We finally observe that we shall restrict ourselves here to consideration of slow blood

velocities, which are known to normally occur in small blood vessels, as well as in large ones when some pathological circumstances concur.

The results herein obtained hint at the possibility of developing a procedure to monitor tissue pathological processes leading to intravascular blood coagulation by means of ultrasound techniques. A discussion on the results obtained, the limitations of our approach, and possible future directions, is gathered in our concluding Sect. 5.

2 An activation-polymerization model

We next present our basic, space-dependent mathematical model for activated fibrin polymerization. To put it into a suitable perspective, we first briefly recall some known aspects of the blood coagulation process.

As we already mentioned in the Introduction, blood coagulation is regulated by means of a set of biochemical reactions, usually referred to as the Blood Coagulation Cascade (BCC), which involves a number of extremely efficient positive and negative feedback loops. Two components are usually distinguished in such a cascade, namely the so-called Extrinsic and Intrinsic pathways [4,5,25–27] which interact at various levels, and eventually converge to produce thrombin. The latter is a key activating substance that acts on inactive fibrinogen to produce actively polymerizing fibrin molecules. Our current knowledge of the reactions involved in the BCC includes over thirty species, and due to the complexity of its structure, it is customary to represent the BCC by means of (rather complicated) graphic diagrams [4,5,16,26].

A mathematical description of the BCC requires a large number of differential equations, involving an even larger set of kinetic parameters, so that the resulting system is often unwieldy for simulation purposes. Moreover, a degree of uncertainty remains concerning the actual values of the parameters involved. On the other hand, maintaining a high level of complexity in the model does not necessarily ensure a high accuracy in the results obtained from its simulation. As a matter of fact, it is known that, even for models with a comparatively simple structure (say, no more than five equations), the same kinetic curve of thrombin behavior may be derived from different sets of selected kinetic constants [10]. In view of these remarks, the use of simplified models seems quite appropriate, as long as the information derived form their analysis and simulation yield useful insight into the process under consideration.

Bearing these points in mind, and with a view towards describing the appearance of externally induced microthrombi clouds in a vessel, we now propose a phenomenological model that takes into account the effects of thrombin production, anticoagulant agents (i.e., inhibitory pathways), and fibrin polymer formation upon fibrinogen activation [6,7,12] combined with mass-transport processes corresponding to diffusion and convection. This model reads as follows:

$$\frac{\partial \theta}{\partial t} = \frac{\alpha \theta^2}{\theta + \theta_0} - \chi_1 \theta - \gamma \theta \varphi + \kappa + D_\theta \Delta \theta - \nabla(v\theta), \tag{2.1}$$

$$\frac{\partial \varphi}{\partial t} = \beta \theta \left(1 - \frac{\varphi}{c}\right)\left(1 + \left(\frac{\varphi}{\varphi_0}\right)^2\right) - \chi_2 \varphi + D_\varphi \Delta \varphi - \nabla(v\varphi), \tag{2.2}$$

$$\frac{\partial F_g}{\partial t} = -k_g F_g \theta - \varepsilon_g \left(F_g - F_g^0\right) + D_g \Delta F_g - \nabla\left(v F_g\right), \tag{2.3}$$

$$\frac{\partial F_1}{\partial t} = k_g F_g \theta - k_p F_1 \sum_{i=1}^{\infty} a_{1i} F_i + k_b \sum_{i=1}^{\infty} b_{1i} F_{i+1} - k_r F_1 + D_1 \Delta F_1 - \nabla(v F_1), \tag{2.4}$$

$$\begin{aligned}\frac{\partial F_k}{\partial t} = {} & \frac{k_p}{2} \sum_{m=1}^{k-1} a_{m(k-m)} F_m F_{k-m} - k_p F_k \sum_{i=1}^{\infty} a_{ki} F_i + k_b \sum_{i=1}^{\infty} b_{ki} F_{k+i} \\ & - \frac{k_b}{2} \sum_{i+j=k} b_{ij} F_k - k_r F_k + D_k \Delta F_k - \nabla(v F_k), \quad k = 2, 3, \ldots.\end{aligned} \tag{2.5}$$

In the previous set of equations, θ denotes the concentration of polymerization activator (thrombin), φ that of an inhibitor (anticoagulant) which acts as an antagonist to the former, F_g stands for fibrinogen concentration, F_1

represents the concentration of fibrin monomers, and F_i denotes concentration of fibrin polymers with i components (i-mers) where $i = 2, 3, \ldots$ On the other hand, v is the velocity of blood flow, and the various parameters appearing in (2.1)–(2.5) correspond to kinetic reaction constants and diffusion coefficients. Note that space dependence is explicitly included in (2.1)–(2.5). We next describe briefly the way in which system (2.1)–(2.5) has been derived.

To begin with, we remark that the equations (2.1)–(2.5) can be seen as consisting of two coupled modules representing different processes. The first one, consisting in (2.1) and (2.2) yields a regulated production of thrombin, which acts as an injection source in the second module, represented by (2.3)–(2.5). The latter accounts for the transformation of fibrinogen into fibrin monomers (see (2.3)), which in turn undergo a polymerization process (cf. (2.4) and (2.5)).

Consider the first module above. In our approach, Eqs. 2.1 and 2.2 provide a phenomenological reduction of the whole set of reactions leading to thrombin production. This two-variable module, which can be thought of as a minimal model of the biochemical cascade, was introduced in [6,7] in the space-independent case, and has an activator–inhibitor structure, similar to that introduced by Turing in [28] and by Gierer and Meinhardt in [29] in the linear and nonlinear cases, respectively (see [30, Chaps. 2 and 3], for a detailed discussion on the latter). The only variables therein retained are, respectively, the concentration of thrombin and that of a generic inhibitor thereof. The latter has to be understood as a substance representing an averaged effect of the negative feedback loops (in which activated protein C is widely assumed to play a key role) that are in part activated by thrombin itself and in turn control thrombin production [6–8].

Concerning the precise structure of these equations, note that (2.1) can be viewed as a modified KPP–Fisher equation (see [31, Chap. 11.2], [32,33]). When $\theta \gg \theta_0$, and $v = 0 = \gamma = \kappa = 0$, the resulting version of (2.1) is such that any overcritical perturbation of the rest state leads to linear autocatalytic production of θ. On the other hand, Eq. 2.2 corresponds to a different dynamics, this time of a bistable type, which is modulated by thrombin concentration θ; cf. the first term in the right in (2.2). Bistability in (2.2) describes a situation in which two stable equilibria, separated by an unstable one, are possible. According to this picture a small perturbation in the smaller stable state is quickly damped out, but a sufficiently large one switches the dynamics to a neighborhood of the larger stable state. In this manner, the inhibitor limits the otherwise unbounded growth of thrombin through the effect of the third term in the right-hand side of (2.1). The coupled system consisting of (2.1), (2.2) thus provides an example of an excitable system, the latter being a basic building block in the modeling of biological processes; for a review, see [34, Chap. 3, pp. 32–80]. The system (2.1)–(2.2) has been shown to reproduce key aspects of pattern formation in blood coagulation, including in particular localization of haemostatic clot formation (see for instance [8,35]). Excitability is readily shown from analysis of the phase portrait of the kinetic (i.e, space-independent) version of the system (2.1)–(2.2); cf. [12].

The link between thrombin activation and fibrin polymerization is established by means of the fibrinogen equation (2.3) in the second module of our system. Fibrinogen conversion acts in turn as a forcing term in the polymerization equations (2.4), (2.5). We assume there that fibrin polymerization occurs in accordance with a standard coagulation–fragmentation mechanism involving an infinite system of coupled nonlinear differential equations. The coagulation part is described by means of the classical Smoluchowski formalism [36,37], [38, Chap. 8, pp. 222–248], except for the fact that the coagulation coefficients a_{ij} are of a Flory–Stockmayer type [11,39–41],

$$a_{ij} = ((f-2)i + 2)\,((f-2)j + 2)\,, \quad i, j \geq 1, \tag{2.6}$$

where f denotes the functionality (related to the polymerization capability) of the monomers being considered. In the case of fibrin, it is known that $f = 4$ [42]. Since this value is larger than two, the process under consideration can eventually lead to a sol–gel phase transition, characterized by the onset at a finite time of a gel phase [39]. This is often described in an informal, but illuminating, manner as an infinitely long molecule which is a sink for polymers in the sol fraction which does not contribute back to the reaction [43]. Fragmentation effects are represented by the coefficients b_{ij} in (2.4), (2.5), which are introduced to include reversibility in the formation of polymer chains (see [41] and [44] for more details). As observed in [12], where the space-independent version of system (2.1)–(2.5) has

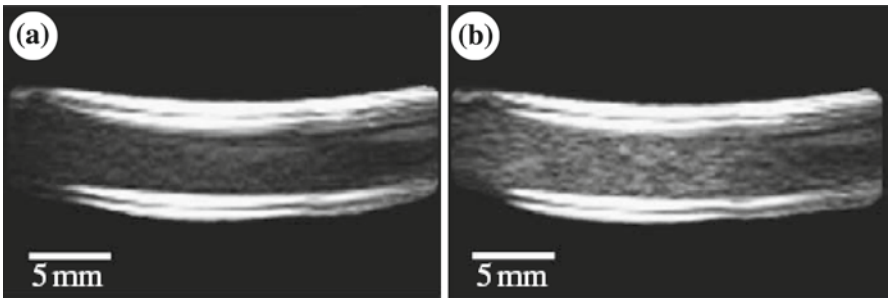

Fig. 1 Ultrasonic images of blood flow in a vessel **a** before and **b** after microthrombi formation. Reproduced from [16]

been studied, a relevant choice for the case under consideration consists in taking b_{ij} to be constant. In particular, the value

$$b_{ij} = 2 \tag{2.7}$$

is compatible with the so-called normalization condition for fragmentation [44] and will be retained henceforth. Under such assumptions, the kinetic, space-independent version of (2.1)–(2.5) has been shown to develop polydisperse fibrin mixtures, that can lead to a sol–gel phase transition depending upon ranges of the associated parameters [12].

Having described our basic model system, we now turn our attention to the way in which experimental information on the process under consideration can be obtained.

3 Ultrasound detection of microthrombi formation

In recent times, an experimental method has been developed for early diagnostics of pathologies in blood coagulation by means of ultrasound techniques [15,16]. The latter are widely used in clinical practice to determine the structure and performance of internal organs. In short, the operating procedure consists in sending ultrasound (US) waves to the selected target by means of a transducer (a device transforming electrical input into acoustic radiation), and then measuring the resulting backscattering echo effects. In general, two-dimensional (termed B-mode) images are obtained by means of a combination of echoes received along different straight lines [45].

When moving structures, such as microthrombi, are present in blood flow one has to deal with backscattered signals arising from multiple moving scatterers. A common way to analyze such a situation consists in estimating the integrated power of the Doppler shift spectrum [46, Chap. 10], [16]. In this manner, one eventually obtains images as those shown in Fig. 1.

The onset of smoke-resembling clouds as seen in Fig. 2b corresponds to the presence of heterogeneities associated to microthrombi. This is sometimes referred to as a snowstorm pattern [14,18]. We maintain that the formation of such structures corresponds to an early stage of blood coagulation, when fibrin monomers and short polymers (of no more than about 0.1 mm in size) appear, but large aggregates have not been formed, and there is no macroscopic fibrin gel yet.

We are interested in characterizing microthrombi detection by means of suitable functions (moments of polymer concentrations) whose values can be obtained from analysis of the mathematical model described in the previous section. More precisely, let us denote by F_n the concentration of fibrin polymers consisting of n monomer units. Then the moment of order k ($k = 0, 1, 2, \ldots$) of the polymer distribution is given by [12]:

$$M_k = \sum_{n=1}^{\infty} n^k F_n \tag{3.1}$$

The distribution of moments thus obtained is an ordered one, so that $M_0 \leq M_1 \leq M_2 \leq \cdots$. The moment of first order M_1 represents the total normalized mass of polymer in the system. The second-order moment M_2 is an

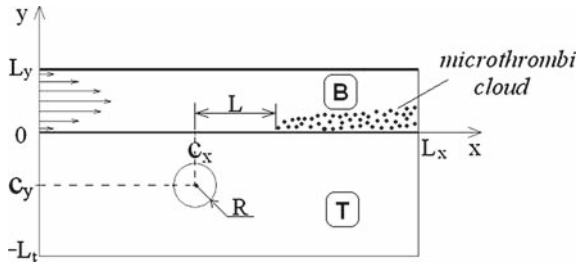

Fig. 2 Representation of the spatial setting of the model. Region B corresponds to a blood vessel and region T corresponds to an adjacent tissue region. The length of the blood vessel is L_x and its diameter is L_y. The sizes of the tissue domain are L_x and L_t. There is a blood flow inside the vessel, and its profile is schematically shown by *arrows* in the left part of region B. The tissue contains a source of activation (the corresponding domain is indicated by a *circle*). The center of that source has coordinates (c_x, c_y)

indicator of the degree of polymerization of the process under consideration. The ratio M_2/M_1 is in turn related to the "weight-averaged" molecular weight of polymer molecules [47, part 3.7]. More precisely, there holds:

$$\langle \mu_w \rangle = m_0 \frac{M_2}{M_1} \tag{3.2}$$

Where $\langle \mu_w \rangle$ denotes the weight-averaged molecular weight of polymer molecules [47, Eq. 3.112], and m_0 stands for the mass of a single monomer unit. In isolated polymer systems displaying a sol–gel phase transition, a standard criterion for gel formation consists in detecting a finite-time blow-up of the second moment M_2, and the time at which such singularity is formed is said to be the gelation time t_g [39,40,48]. Note that, when there is neither monomer injection nor deactivation, M_1 remains constant for times $t < t_g$, so that in accordance with (3.2) blow-up for M_2 and for $\langle \mu_w \rangle$ are equivalent.

On the other hand, it is well known that wave scattering in solutions can be described in terms of the attenuation coefficient (also known as turbidity coefficient in optics) χ, defined by means of the attenuation law:

$$I = I_0 \mathrm{e}^{-\chi l} \tag{3.3}$$

where I_0 and I are the intensities of incident and transmitted waves, and l is the average wavelength path of incident waves [46, Chap. 10]. The attenuation coefficient is proportional to the averaged molecular weight $\langle \mu_w \rangle$ and to the mass concentration C, where $C = N_A m_0 M_1$. More precisely (see [47, Eqs. 3.107 and 3.108]) one has:

$$\chi = \frac{8\pi}{3} H (N_A m_0 M_1) \langle \mu_w \rangle \tag{3.4}$$

where:

$$H = \frac{4\pi^2 n_0^2}{\lambda^4 N_A} \left(\frac{\mathrm{d}n}{\mathrm{d}C} \right)^2 ; \tag{3.5}$$

here n and n_0 are the refractive indexes of solution and pure solvent, N_A is Avogadro's number, and λ is the signal wavelength. Recalling (3.2), we observe that the attenuation coefficient is proportional to the second moment M_2:

$$\chi = \text{const} \cdot \frac{1}{\lambda^4} M_2 \tag{3.6}$$

with $\text{const} = 8\pi/3 \cdot (2\pi n_0 m_0 \mathrm{d}n/\mathrm{d}C)^2$. A relation between the second moment of the fibrin polymer distribution and a parameter that can be measured by means of ultrasound techniques is thus obtained.

When using actual transducers, the backscattered attenuation observed depends on the technical specifications of the device employed. In particular, for any transducer, a critical value of the attenuation coefficient χ_{cr} exists, which is characterized as follows. If the medium has an attenuation coefficient larger than χ_{cr}, then backscattered effects allow to identify absorbing structures in that medium, which correspond to a solution of particles having a second moment larger than some critical value M_{cr}. This is obtained from χ_{cr} through (3.6). If, however, the attenuation coefficient is lower than χ_{cr}, then such a medium appears as transparent. A typical value for the critical attenuation coefficient is $\chi_{\mathrm{cr}} < 10^{-3}\,\mathrm{cm}^{-1}$ [46, Chap. 10].

4 On the location of an externally induced microthrombi cloud

In this section we shall complete the formulation of our mathematical model to account for externally induced activation of fibrin polymerization, and analyze the way in which the details of a such process play a role in the selection of critical values for the moments of polymer distributions.

4.1 Including external activation in the model

We will suppose that there is a substance, whose concentration is denoted by u, which is produced in a tissue, which activates the cascade of thrombin production when it leaks into a blood vessel. This substance is generated as a byproduct of a pathological process, is distributed in tissue by diffusion, and may go through the vessel wall to appear in the blood flow, to act as primary activator of intravascular blood coagulation. The sources of such primary activators may be tumor cells (producing cancer procoagulants [49]), bacteria, virus-infected cells or immune cells of the organism. In the latter case leucocytes are known to produce cytokines, capable to reach into the blood flow and to activate blood coagulation [20,21]. Such substances usually trigger blood coagulation by activating the so-called extrinsic biochemical pathway [50, Chap. 5B]. We shall assume that the distribution of u in tissue takes place according to an equation of reaction–diffusion type [29], [30, Chaps. 2, 3, pp. 11–24], [31, Chaps. 9, 11–14.4]:

$$\frac{\partial u}{\partial t} = F(u) + D_T \Delta u \tag{4.1}$$

where function $F(u)$ describes the kinetics of u according to the underlying-tissue pathological process. Equations as (4.1) are widely used to describe self-sustained spatial distribution of chemical signals [31, Chap. 11], [29,51], [52, Chaps. 9–10, pp. 268–311] as well as tumor progression [53]. In the following, we shall assume that the function $F(u)$ is of bistable type. More precisely, we assume that there are two stable states: $u = 0$ when the pathological source is not active and $u = 1$ when it is active. Both stable states are separated by an unstable one. Specifically, we will take $F(u)$ to be of Zel'dovich and Frank–Kamenenetzki type [31, Chap. 11.6, p. 304], [34,54]:

$$F(u) = k_1 u\,(1-u)\,(u-a)\,, \quad 0 < a < 1. \tag{4.2}$$

Notice that for $a < u < 1$, $F(u) > 0$ and u increases to converge to the stationary state $u = 1$; whereas for $0 < u < a$, $F(u) < 0$ and consequently u decreases in this interval to approach towards the stationary state $u = 0$. The region in tissue where $u > a (F(u) > 0)$ is assumed to correspond to the location of a tissue pathological source (TPS). It is known that (4.1), (4.2) is able to produce wave-like solutions of a front type that link the spreading stable state $u = 1$ to the receding stable state $u = 0$, and that the wave velocity is given by $v_T = \sqrt{2 D_T k_1}\,(0.5 - a)$ [34, Chap. 2.2, pp. 18–23]. In most of the numerical experiments to follow, a was assumed to be equal to 0.2, whereas the value of k_1 has been taken as to fit to relevant growth velocities of tissue pathological sources [53].

On the other hand, it will be assumed that the parameter κ in (2.1) is directly proportional to the concentration of that substance:

$$\kappa = k_u u. \tag{4.3}$$

The value of parameter k_u may depend upon the nature of any specific pathological substance (u) generated in tissue; particular values for it will be selected in the next Sect. 4.2. In its turn, the concentration in blood of such a primary activator u changes according to a general equation of reaction–diffusion–convection type [55]:

$$\frac{\partial u}{\partial t} = -k_d u + D_u \Delta u - \nabla (v u). \tag{4.4}$$

The geometry of the problem to be considered is depicted in Fig. 2.

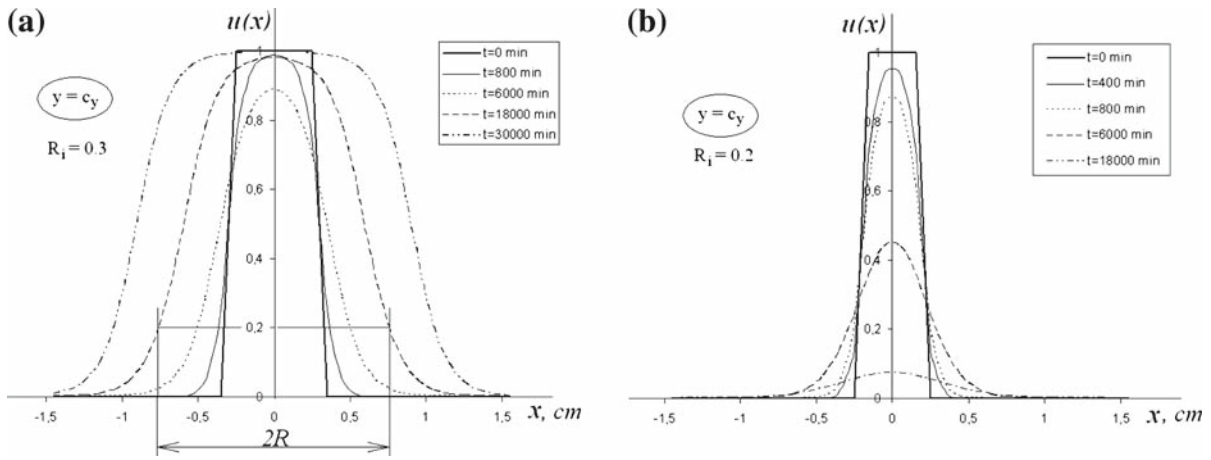

Fig. 3 Profiles $u(x, c_y, t)$ of the tissue-agent distribution at different times. The initial distribution was set to unity in a region of radius R_i and zero elsewhere. **a** Overcritical initial radius $R_i = 0.3\,\text{cm}$. **b** Subcritical initial radius $R_i = 0.2\,\text{cm}$. $R(t)$ is shown for several times up to 30,000 min

Equations 4.1 and 4.4 are linked by boundary conditions on the vessel wall that separates the tissue where TPS is located and the vessel under consideration (see Fig. 2). They are taken in the form:

$$-D_T \left.\frac{\partial u}{\partial y}\right|_{y=-0} = \mu\left(u^- - u^+\right), \tag{4.5}$$

$$-D_u \left.\frac{\partial u}{\partial y}\right|_{y=+0} = \mu\left(u^- - u^+\right), \tag{4.6}$$

where u^- (respectively, u^+) denotes the limit of u as the vessel wall is approached from the tissue side (respectively, from the vessel side), D_T (respectively, D_u) represents the diffusion coefficient in tissue (respectively, in blood), and μ is a permeability parameter. The value of parameter μ will be taken smaller than D_T/H (H being the characteristic thickness of the vessel wall) to reflect the barrier function of the latter.

For bistable-type propagation as that assumed for the primary activator, it is well known that the onset of wave propagation of the substance thus produced (but not its asymptotic wave speed) depends on the initial conditions. More precisely, a critical size of the initial perturbation R_{cr} exists, which is related to the threshold value a in (4.2), and is such that for an initial size R_i with $R_i < R_{\text{cr}}$, the pathological area shrinks with time, whereas for $R_i > R_{\text{cr}}$, such a region grows in time, and its front asymptotically propagates in a sustained manner as a traveling wave [55–58], [34, Chap. 2.2, pp. 18–23]. We illustrate this situation by means of the following example. Consider the case where the center of the TPS is located at the point $(x, y) = (c_x, c_y)$, and the initial conditions are:

$$u = \begin{cases} 1 & (x-c_x)^2 + \left(y-c_y\right)^2 \le R_i^2 \\ 0 & (x-c_x)^2 + \left(y-c_y\right)^2 > R_i^2. \end{cases} \tag{4.7}$$

Then the spatio–temporal behaviour of variable u satisfying (4.3), (4.4) with $a = 0.2$ can be numerically computed and is represented in Fig. 3.

For definiteness, the radius R of the pathological source was selected as the half-width of the region where $u(x, c_y, t) > a$. The dependence of that radius on time for different values of the initial perturbation R_i is shown in Fig. 4.

It follows from Fig. 4 that the critical radius R_{cr} is approximately equal to $0.25 \pm 0.05\,\text{cm}$ in this case. When the initial condition (4.7) is such that $R_i \ge R_{\text{cr}}$, the size of the region with enhanced concentration of u increases. The asymptotic velocity of wave propagation is independent of the selected initial value of R_i, as predicted by theoretical results [34, Chap. 2], [59, Sects. 0.4 and 0.5, pp. 18–26].

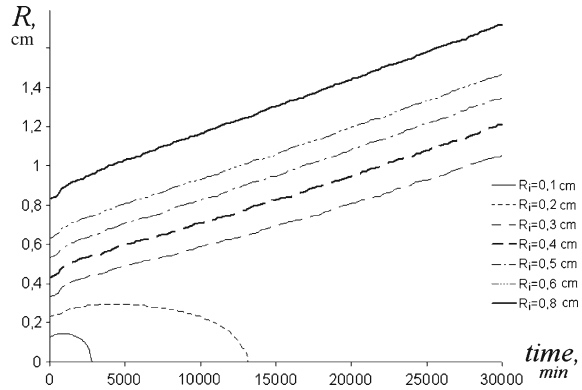

Fig. 4 Radius of tissue pathological source as a function of time

Concerning the time scale used in Figs. 3 and 4, a few remarks are in order. In those pictures, tissue pathology is kept track of for up to 30,000 min, which is more than 20 days. This is a long period when compared with the time scale of blood coagulation (which is usually of the order of seconds to minutes). However, for many tumors, 20 days represent a very early stage of development, during which they remain fully asymptomatic, and the disease cannot be detected by standard medical tests. Roughly speaking, what we are considering in Figs. 3 and 4 is the recent history of TPS activity. As far as blood coagulation induced by that process is activated on a very low level, we may talk about early stages of blood coagulation, when no macroscopic thrombi are formed yet. On the other hand, choosing such slow tissue processes as those considered in this work allows us to deal with quasi-stationary induced microthrombi clouds at each stage of the existence of TPS.

Other choices of time scales are possible indeed. For instance, the situation when the characteristic times of tissue process and blood coagulation are comparable will be of practical interest when dealing with traumatic tissue and vessel wall injury, a case which is not addressed in this work.

4.2 A simplified model for intravascular microthrombi detection

A quick glance at (2.1)–(2.5) and (4.1)–(4.6) reveals at once that such a system is quite involved for analytical treatment. We next obtain a simplified model amenable to mathematical analysis and numerical simulation, while at the same time retaining substantial features of the process under consideration that could be related to ultrasound experiments. To proceed further, we assume that the diffusion coefficients do not depend upon polymers length:

$$D_k = D = \text{const}, \quad \text{for all } k. \tag{4.8}$$

While it is natural to expect that polymer diffusivities should depend on polymer size, the simplifying assumption (4.8) is still a reasonable one when short-length polymers are considered, as is the case for early polymerization stages of the kind considered in this work. Using (3.1) and (4.8) we may easily to transform (2.4)–(2.5) into a form which includes the following three equations for the first moments:

$$\dot{M}_0 = k_g F_g \theta - 2k_p (M_1 + M_0)^2 + k_b (M_1 - M_0) - k_r M_0 + D\Delta M_0 - \nabla(v M_0), \tag{4.9}$$

$$\dot{M}_1 = k_g F_g \theta - k_r M_1 + D\Delta M_1 - \nabla(v M_1), \tag{4.10}$$

$$\dot{M}_2 = k_g F_g \theta + 4k_p (M_2 + M_1)^2 - \frac{k_b}{3}(M_3 - M_1) - k_r M_2 + D\Delta M_2 - \nabla(v M_2). \tag{4.11}$$

As a matter of fact, the transformed system of equations is an infinite one, and is not in a closed form. By this we mean that the equation for any given moment includes moments of higher order, a fact which comes as a consequence of the fragmentation terms retained in the model. As we have done previously in [12], we reduce (4.9)–(4.11) to a well-posed problem by introducing the closure assumption:

$$M_1 M_3 - M_2^2 = 0. \tag{4.12}$$

Notice that (4.12) is exactly satisfied when the whole polymer fraction is distributed in monomers or in polymers of the same size (monodisperse distributions). In all remaining cases, one always has that the left-hand side in (4.12) is larger than the right-hand side, so that upon substitution in (4.11), we obtain a subsolution for the second moment. In particular, by a comparison argument, it then follows that, whenever this subsolution blows up, so does the second moment itself.

Closure assumptions are widely used in fluid dynamics. A paramount example is provided by turbulent flows, where the velocity and pressure of a fluid are often divided into their averaged and fluctuating parts. When these are substituted in the corresponding fluid equations, one ends up with systems involving more unknowns than equations, since some of the correlation terms appearing therein remain undetermined at any stage. This is the classical closure problem for Reynolds equations, which has led to an extensive literature in the theory of fluid motions [60, Chap. 7]. It is usually addressed by imposing closure assumptions, as we have done before.

Taking into account (4.12), we may reduce the system (4.9)–(4.11) to:

$$\dot{M}_0 = k_g F_g \theta - 2k_p (M_1 + M_0)^2 + k_b (M_1 - M_0) - k_r M_0 + D\Delta M_0 - \nabla (v M_0), \tag{4.13}$$

$$\dot{M}_1 = k_g F_g \theta - k_r M_1 + D\Delta M_1 - \nabla (v M_1), \tag{4.14}$$

$$\dot{M}_2 = k_g F_g \theta + 4k_p (M_2 + M_1)^2 - \frac{k_b}{3}\left(\frac{M_2^2}{M_1} - M_1\right) - k_r M_2 + D\Delta M_2 - \nabla (v M_2). \tag{4.15}$$

To perform suitable numerical simulations, these equations have to be supplemented with initial and boundary conditions. On the vessel walls we impose no-flux conditions, namely:

$$\left.\frac{\partial \theta}{\partial y}\right|_{y=0} = \left.\frac{\partial \varphi}{\partial y}\right|_{y=0} = \left.\frac{\partial F_g}{\partial y}\right|_{y=0} = \left.\frac{\partial M_0}{\partial y}\right|_{y=0} = \left.\frac{\partial M_1}{\partial y}\right|_{y=0} = \left.\frac{\partial M_2}{\partial y}\right|_{y=0} = 0, \tag{4.16}$$

$$\left.\frac{\partial \theta}{\partial y}\right|_{y=L_y} = \left.\frac{\partial \varphi}{\partial y}\right|_{y=L_y} = \left.\frac{\partial F_g}{\partial y}\right|_{y=L_y} = \left.\frac{\partial M_0}{\partial y}\right|_{y=L_y} = \left.\frac{\partial M_1}{\partial y}\right|_{y=L_y} = \left.\frac{\partial M_2}{\partial y}\right|_{y=L_y} = 0. \tag{4.17}$$

Boundary conditions on the left boundary of the blood vessel are selected as follows:

$$\theta|_{x=0} = 0 \quad \varphi|_{x=0} = 0 \quad F_g|_{x=0} = F_g^0 \quad M_i|_{x=0} = 0, \quad i = 0, 1, 2. \tag{4.18}$$

At the exit of the vessel we assume that no perturbation of the solutions appear in a neighborhood of the right boundary of the vessel. Under this assumption we may use a linear extrapolation of the solution in the boundary points, where the solution cannot be found from the equations. Linear extrapolation implies that the second-order derivatives are set equal to zero:

$$\left.\frac{\partial^2 \theta}{\partial x^2}\right|_{x=L_x} = \left.\frac{\partial^2 \varphi}{\partial x^2}\right|_{x=L_x} = \left.\frac{\partial^2 F_g}{\partial x^2}\right|_{x=L_x} = \left.\frac{\partial^2 M_1}{\partial x^2}\right|_{x=L_x} = \left.\frac{\partial^2 M_2}{\partial x^2}\right|_{x=L_x} = 0. \tag{4.19}$$

This approach is commonly used, for example, in hydrodynamic numerical simulations [61, Chap. 10.3.5, p.459].

As to the velocity of blood flow in the vessel, it is assumed to follow the well-known Poiseuille–Hagen equation for fully developed laminar flow [60,62,63]:

$$v_x(y) = \frac{4 v_{\max}}{L_y^2} y \left(L_y - y\right), \quad v_y = 0, \tag{4.20}$$

where the parameter L_y refers to vessel diameter, and $v_{\max}$ denotes the mid-stream velocity. It is known that in large vessels of healthy persons (diameter $0.5 \div 1.5$ cm), $v_{\max}$ may reach up to 40–50 cm/s in the aorta, to remain generally between 5–15 cm/s in other comparatively large vessels; see [64, Chap. 20.4]. However, in many pathologies dealing with ischemia, blood-flow velocity is drastically lowered, particularly in elderly patients [65, Chap. 7], [66, Unit IV]. Actually, blood-flow velocity may decrease, for instance, in the case of increased viscosity that may happen if hematocrite (concentration of red cells) of blood goes beyond its normal value. It is well known that, if hematocrite is increased up to 56% (instead of its normal proportion of 40%), the viscosity value increases up to four times [64, Chap. 20.1]. On the other hand, the blood velocity significantly diminishes in vessels

Table 1 Values of parameters used in numerical simulations

Parameter	Value	Units	Ref.
α	2	min^{-1}	[7,8,67]
θ_0	5	nM	[7,8,67]
χ_1	0.05	min^{-1}	[7,8,67]
γ	5	$(\text{nM min})^{-1}$	[7,8,67]
β	1.5×10^{-3}	min^{-1}	[7,8,67]
c	5	nM	[7,8,67]
φ_0	0.05	nM	[7,8,67]
χ_2	0.35	min^{-1}	[7,8,67]
k_g	3×10^{-4}	$(\text{nM min})^{-1}$	[7,8,67]
F_g^0	9×10^3	nM	[64]
$D_\theta = D_\varphi = D_g = D_u = D$	2×10^{-5}	cm^2/min	[68]
D_T	6×10^{-6}	cm^2/min	[69,70]
μ	2×10^{-4}	cm/min	
L_x	15	cm	
L_y	1	cm	
L_t	3	cm	

containing atherosclerotic plaques. In elderly patients atherosclerosis development often results in stenosis. In many cases the degree of diminishing of the vessel diameter is up to 60–70%. Since resistance to blood motion is known to grow as the fourth power of the vessel radius [64, Chap. 20.1], it turns out that such resistance may increase over 40 times under such conditions. Thus, in such cases, at least in the venous part of the human cardiovascular system, the corresponding blood flow will be significantly slowed down with respect to its normal values. In this work we shall reduce ourselves to situations when the velocity of blood flow is comparatively slow, viz. of the order of no more than 10 cm/min.

In the absence of a primary activator ($u = 0$) blood is in its normal (liquid) state, and there are no activated blood coagulation factors at all:

$$\theta = \varphi = F_i = 0, \quad i = 1, 2, 3, \ldots. \tag{4.21}$$

The concentrations of pre-existing factors (particularly, of fibrinogen) are set to their basal levels:

$$F_g = F_g^0. \tag{4.22}$$

The values of the parameters used in numerical simulations are represented in Tables 1 and 2. The value of parameter α characterizes the speed of overcritical thrombin generation in human plasma. Parameter χ_1 refers to the rate of thrombin inactivation by antithrombin-III molecules. The value of θ_0 is determined by the thrombin destabilization threshold, θ_{cr} ($\theta_0 = \theta_{\text{cr}} \cdot (\alpha - \chi_1)/\chi_1$). Parameter γ reflects the decrease of thrombin production due to the action of anticoagulant, denoted as φ (presumably, activated protein C). The values of β, c, φ_0 and χ_2, respectively, reflect the properties of anticoagulant activation and inactivation [8,67].

The values of the parameters k_r and k_b are derived from basal levels of plasmin and factor XIII_a in human blood. Plasmin is the most important fibrinolytic agent [50, Chap. 8], [64, Chap. 18.6]. In terms of our model, the larger the concentration of plasmin is, the larger the value of parameter k_r should be. On the other hand, factor XIII_a is known to act as a fibrin-polymer stabilizing factor [50, Chap. 8], [64, Chap. 18.6]. Association of factor XIII_a-molecule with fibrin-polymer significantly reduces the rate of the fragmentation process (i.e. k_b). More precisely, the values of k_r and k_b represented in Table 2 refer to averaged values of plasmin and factor XIII_a concentrations in human blood ($[\text{FXIII}] = 10^5$ nM, $[\text{Plasmin}] = 1.5 \times 10^3$ nM). We should point out that the value $k_b = 3.8\,\text{min}^{-1}$ selected by

Table 2 Values of parameters used in numerical simulations and their comparison with some literature sources

Parameter	Units	Weisel et al. [72]	Hantgan and Hermans [73]	Lewis et al. [71]	Parameters selected
k_g	$(\mathrm{nM\,min})^{-1}$	3×10^{-4}	0.5×10^{-4}	0.65[a]	3×10^{-4}
k_p	$(\mathrm{nM\,min})^{-1}$	4×10^{-3}	50×10^{-3}	$(3 \div 60) \times 10^{-3}$[a]	15×10^{-3}
k_b	min^{-1}			3.8[b]	0.1
k_r	min^{-1}				7

[a] The reaction rates were estimated for the process of fibrinopeptide A release only and corresponding polymerization
[b] The value $k_b = 3.8\,\mathrm{min}^{-1}$ was estimated for a system where no factor XIII is present

Lewis et al. [71] (see Table 2) has been obtained on the basis of the so-called biochemical "reconstructed" system, containing no factor XIII.

The values of the rate constants k_g and k_p used in this paper (see Table 2) have been determined in accordance with theoretical and experimental data presented in [11,71–73]. In fact, both rate constants depend on the ionic strength of the solution [71]. The values of k_g and k_p given in accordance with experiments by Lewis et al. [71] have been determined on the basis of fibrinopeptide A (FPA) release. However, when fibrinogen converts into fibrin, not only FPA but also fibrinopeptide B is released [50, Chap. 8]. This is why in the present paper we use slightly different values of rate constants with respect to values estimated in previous works (see Table 2). On the other hand, since the characteristic time of fibrinogen restoring is on average of about 10^2 h [50, Chap. 8], we suppose that the value of ε_g is equal to $10^{-4}\,\mathrm{min}^{-1}$.

The characteristic time of primary activator degradation ($\tau_d = 1/k_d$) varies from a few hours to some days. This means that the relevant rate constant k_d may be taken to be smaller than $10^{-3}\,\mathrm{min}^{-1}$. In the numerical simulations to follow, the rate constants k_d and ε_g have been assumed to be of the same order and equal to $10^{-4}\,\mathrm{min}^{-1}$. Further precision in our choice of these parameters will be achieved as follows. For simulation purposes, we shall deal with vessels of length $L_x = 15\,\mathrm{cm}$. Under this assumption, and since the blood velocity is quite small near the vessel boundaries, full renewal of blood in the vessel would take about 15 min. Thus, any process characterized by a rate constant lower than $1/(15\,\mathrm{min}) = 0.7 \times 10^{-1}\,\mathrm{min}^{-1}$ may be considered in quasi-static approximation. This suggests that the results of our numerical simulations should be insensitive to any variations of the rate constants k_d and ε_g as long as they remain smaller than $10^{-2}\,\mathrm{min}^{-1}$.

The parameters characterizing the growth of the underlying tissue pathological process (cf. (4.1)) were estimated using information about tumor progression [53,74]. Many theoretical works assume that the speed of tumor-growth progression is of the order of 1–2 μ/h [53,74]. In fact, pathological sources may grow in size with a speed of up to 25 μ/h. Estimating the speed by means of the formula $v_T = \sqrt{2 D_T k_1}(0.5 - a)$ (see Sect. 4.1), we found that a relevant value of k_1 should be no more than $3.5 \times 10^2\,\mathrm{h}^{-1}$.

Finally, in our setting, the parameter k_u connecting tissue and intravascular processes (intensity of initiation of coagulation by primary activator) has a natural limitation. If it is too large, it leads to very rapid coagulation and appearance of gelation, i.e., to blow-up of M_2 in a finite time. This situation should correspond to macroscopic thrombi formation, when hydrodynamic characteristics of blood flow are substantially changed. This is beyond the scope of our model, since our analysis is only intended to deal with stages prior to gelation. For this reason, k_u will be assumed to belong to the interval $k_u \in (10^3; 10^4)\,\mathrm{nM\,min}^{-1}$. The range of the values of k_u was selected so that the concentration of the pathological substance u in tissue remains lower than unity; see 4.2.

4.3 Determining the location of a microthrombi cloud

This section contains the results obtained from a simulation of the reduced system consisting of (2.1)–(2.3), (4.4) and (4.13)–(4.15) in blood, and (4.1), (4.2) in tissue. Parameters were selected as in Tables 1 and 2, and as previously discussed.

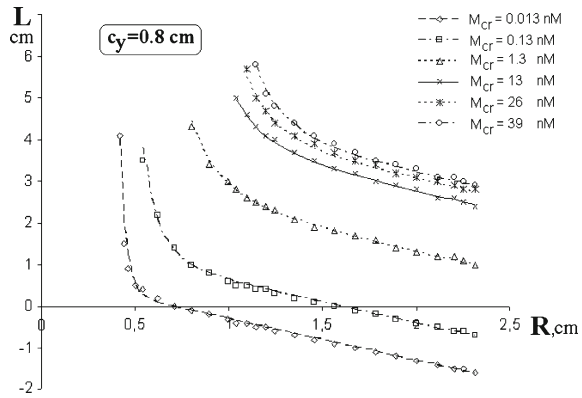

Fig. 5 The function $L(R)$ for different values of $M_{\rm cr}$. $c_y = 0.8\,$cm. If the left edge of the microthrombi cloud is located more proximally than the point $x = c_x$, the shift length L is negative. This explains why for some values of $M_{\rm cr}$ the plots $L(R)$ go beyond zero

The numerical simulation of our model involves coupling two processes with different time-scales. To do this, we proceed as follows. First, the spatial distribution of a slowly evolving, primary activator (u) is computed in time, both in tissue and blood vessel. This can be done, since $u(x, y, t)$ does not depend upon variables describing the blood coagulation status ($\theta, \varphi, F_g, F_1, \ldots$). To keep track of processes unfolding at this slow time scale, appropriate time-steps are used for this simulation. After that, the spatial distribution of primary activator $u(x, y, t)$ was considered as quasi-static (varying in an extremely slow manner in comparison with the blood coagulation process). Each of these distributions was thus used as a stationary pattern of primary activator distribution in the vessel. So, for each time moment we solved separately the problem described by (2.1)–(2.5) using in (2.1) the expression (4.3) with the solution of (4.4) obtained before. The problem described by (2.1)–(2.5) was then simulated until a stationary state of concentrations in the vessel was obtained (usually about 20 min). This system of equations was solved numerically on a uniform rectangular mesh with the aid of a Runge–Kutta fourth-order method [75, Chap. 5]. The results described below were obtained for a mid-stream velocity $v_{\max} = 10\,$cm/min, the center of pathological source in tissue the was set at $c_x = 3\,$cm and initial radius of the tissue pathological source was set $R_i = 0.3\,$cm.

Let us briefly describe the results thus obtained. After blood coagulation is triggered by an external activation, fibrin-monomer intravascular generation occurs. Fibrin polymerization gives rise to an increase of concentrations of fibrin polymers F_i. According to our current approach, we can follow this process by keeping track of the relevant moments M_2. Indeed, bearing in mind our discussion in Sect. 3, we will consider the second moment as a marker for the intensity of echo contrast observed by US in blood vessel. More precisely, the microthrombi cloud in blood flow is defined as the region where

$$M_2 > M_{\rm cr} \tag{4.23}$$

for some critical reference value $M_{\rm cr}$. As remarked in Sect. 3, $M_{\rm cr}$ can be related to technical parameters of the ultrasound transducer used in experimental measurements. We shall assume that no coagulation process, other than the one we are discussing, is taking place in the vessel under consideration. This allows us to suppose that the basal value of the second moment is equal to zero there. As a matter of fact, while the concentration of fibrinogen in blood is comparatively large (about 9,000 nM, or 3 g/l, [64, Chap. 18.6]), the amount of fibrin is negligible, unless BCC is activated.

In our numerical simulations the microthrombi cloud is usually found near the vessel wall, and is generally shifted by blood flow downstream along the x-coordinate with respect to the position of the tissue pathological source (see Fig. 2). To quantitatively describe the position of the microthrombi cloud, we introduce a characteristic length for its location, the shift-length L. This is defined as the distance along the x-axis from the center of the x-projection of TPS on the vessel wall, c_x to the most proximal edge of the microthrombi cloud (see Fig. 2). We investigated the relation between the radius of the tissue pathological source R and the shift-length of microthrombi cloud L. Our results are shown as plots of L versus R in Figs. 5 and 6.

As the radius of TPS grows, the intensity of intravascular coagulation activation rises, the microthrombi cloud enlarges, and its proximal edge moves closer to the beginning of the vessel. Some curves $L(R)$ obtained

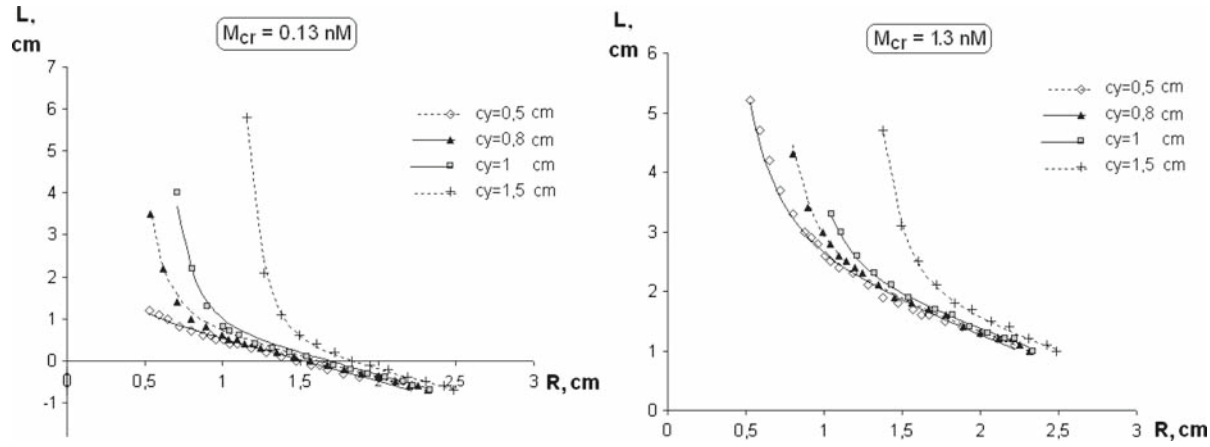

Fig. 6 $L(R)$ for different values of c_y. *Left* $M_{\rm cr} = 0.13$ nM; *right* $M_{\rm cr} = 1.3$ nM

by numerical simulations for given values of $M_{\rm cr}$ are shown in Fig. 5. One can see that the curves for larger $M_{\rm cr}$ lie above the curves corresponding to smaller $M_{\rm cr}$. This fact reflects an obvious property of the system considered: the higher the resolution of the detecting device is, the more fine-grained microthrombi clouds may be detected, and a closer location of microthrombi cloud to TPS is shown to occur.

In Fig. 6 curves $L(R)$ are shown at different distances of TPS from the vessel wall. It is readily seen that the closer the TPS is to the vessel, the smaller is L.

We next proceed to derive a relation between the sizes R and L, irrespective of any particular molecular and/or cellular reasons that might cause the activity of the tissue pathological source. It is clearly seen from Figs. 5 and 6 that each plot of L versus R has at least two different parts: when R is large, this plot appears as a linear one, whereas for R small, the dependence is nonlinear. The simplest formula that may be used to approximate these data is:

$$L = \frac{A}{R^n} - BR + C, \tag{4.24}$$

where the parameters A, B, C and n depend upon parameters of the problem like $M_{\rm cr}$, c_y, k_u, etc. To estimate the set of constants appearing in (4.24), we proceed as follows. For each initial experimental curve $L(R)$, we first approximate its right part (corresponding to large values of R) by means of a linear fit, thus finding the linear formula $\tilde{L} = -BR + C$. In this manner the values of B and C in formula (4.24) are selected by means of a least-squares approximation. We then subtracted $\tilde{L}(R)$ from our initial data $L(R)$. Thus we obtained almost zero values in the right (R large) and non-zero values for R (decreasing for increasing R) for small R when plotting $(L - \tilde{L})$ versus R. To find the parameters A and n we considered only the range of data obtained for R small, plotted them in a doubly logarithmic scale and then used again least-squares approximation.

When written in dimensionless form, Eq. 4.24 has a particularly elegant structure:

$$\frac{\ell_1 - \ell^*}{\ell_2 - \ell^*} = \frac{r_1 - 1/r_1^n}{r_2 - 1/r_2^n}, \tag{4.25}$$

where $\ell = L/R_0$, $r = R/R_0$, $R_0 = \sqrt[n+1]{A/B}$, and $\ell^* = C/R_0$. The values ℓ_1 and r_1 correspond to time t_1, and ℓ_2, r_2 to time t_2. The similarity law (4.25) becomes simpler in some limit cases. For instance, if $r_1, r_2 \ll 1$, one obtains:

$$\frac{\ell_1 - \ell^*}{\ell_2 - \ell^*} = \left(\frac{r_2}{r_1}\right)^n. \tag{4.26}$$

It follows from (4.26) that at the very beginning of tissue pathological source development (that is, for small r) the characteristic dimensionless length of microthrombi cloud shift, ℓ, will decrease in a power-like manner. On the other hand, when $r_1, r_2 \gg 1$, it follows from (4.25) that:

$$\frac{\ell_1 - \ell^*}{\ell_2 - \ell^*} = \frac{r_1}{r_2}. \tag{4.27}$$

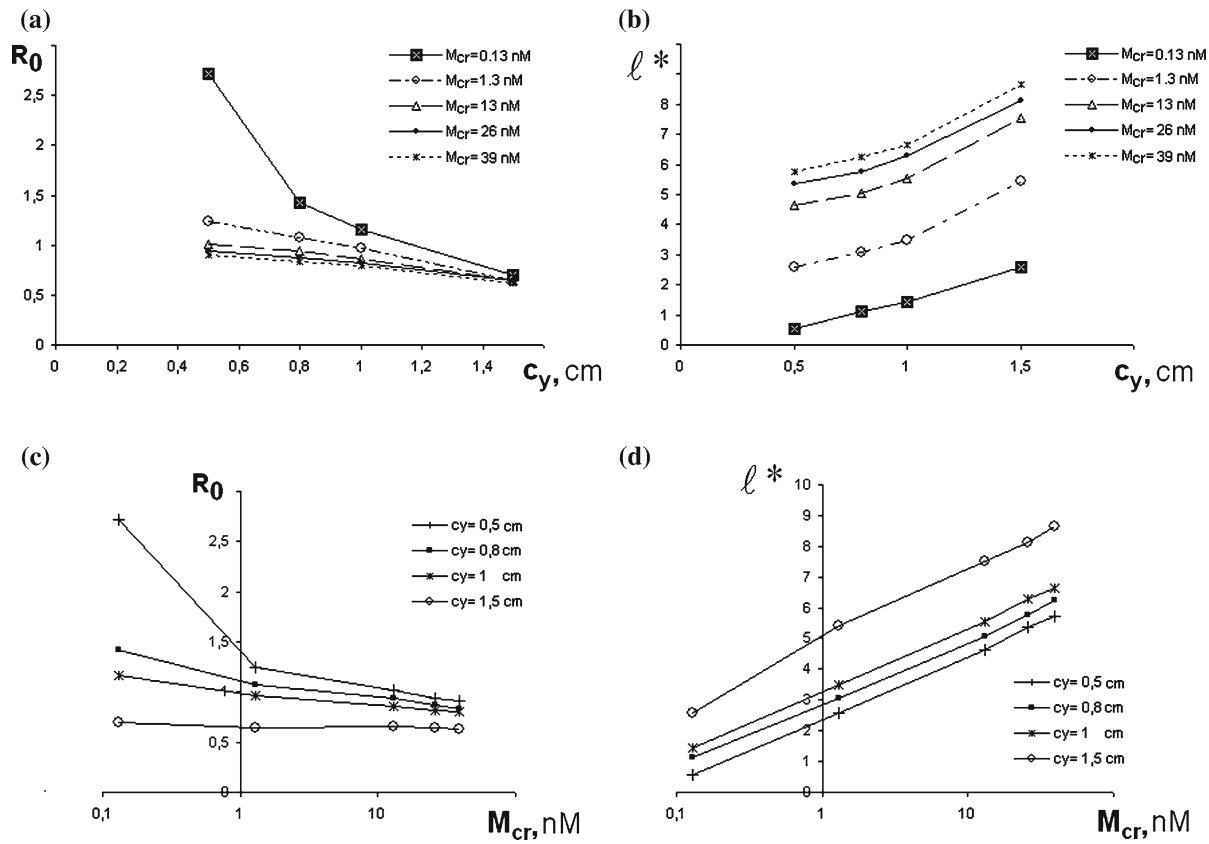

Fig. 7 Plots of the dependence of parameters R_0 and ℓ^* in formula (4.25) upon $M_{\rm cr}$ and c_y. Note that the axis $M_{\rm cr}$ is in logarithmic scale

This relation shows that, if the TPS is well-developed (that is, for $(R/R_0) \gg 1$), the relationship between ℓ and r has a linear form. The dependencies of the parameters ℓ^* and R_0 upon c_y and $M_{\rm cr}$ obtained by means of numerical simulations are shown in Fig. 7.

5 Discussion and concluding remarks

In this paper we have examined a model for intravascular blood coagulation triggered by an external source, which is located at a nearby tissue. A key goal of our approach consists in detecting the early stages of such a coagulation process. These are characterized by the onset of a microthrombi cloud, in which the size of particles of fibrin polymers is quite small. In this way, one would be able to notice an ongoing pathological process at an earlier stage than other diagnostic techniques would do. This is particularly relevant, since such pathologies are known to develop for weeks, months or even years, before any noticeable symptom is felt.

Numerical simulations in our model hint at some general conclusions relating the development of a Tissue Pathological Source (TPS) on one side, and the location of a microthrombi cloud in an adjacent vessel, and induced by the former, on the other. In particular, and for the parameter values selected in Sect. 4, a general similarity law has been proposed; cf. (4.25). This consists in a relation between L (shift length of the microthrombi cloud appearing in blood flow), and the size R of the region where TPS unfolds. Using the limit forms (4.26) and (4.27) of that law, it would be possible to draw conclusions about the stage of the tissue process and its location, in terms of its distance to the vessel wall. Indeed, if the radius of the TPS is very small, and there is no contact yet with the vessel wall, activation of blood coagulation is very weak, and the shift of microthrombi cloud L is very large. At this stage

the plot $L(R)$ decreases very rapidly, much faster than $1/R^2$. This, together with the dependence of our numerical results with respect to c_y (see Fig. 6) shows that, if information about the flow velocity is available, one can draw conclusions not only about the size, but also about the depth of the location of TPS. If the approach sketched here could be fully developed, it might be used in routine non-invasive methods to explore zones of the organism where, for instance, tumors may be located.

It is now worth to discuss some limitations of this work, as well as possible generalizations thereof. To begin with, the appearance of microaggregates in blood flow perturbs the initial hydrodynamic conditions. We have assumed here that this perturbation is small, as in the case of floating admixtures in small concentrations that have little effect on incoming flow. We have also assumed the diffusion coefficients to be independent on polymer length, a hypothesis that needs to be further explored. Moreover, it would be interesting to extend our analysis for velocity values $v_{\max}$ in (4.20) significantly larger than those previously considered, to account for a wider range of blood-flow regimes. Note, however, that many pathological situations are known to exhibit blood-flow velocities considerably smaller than those occurring in healthy individuals [65,66]. Larger blood velocities lead to faster washing out of the microthrombi cloud. Therefore, more intensive activation of blood coagulation is needed in that case to make existence of localized microthrombi clouds possible. Also, additional activation is likely to be required for thrombi to remain attached to the vessel wall. In this paper we have considered the effect of weak activation sources in blood coagulation. In this case, we remain far from macroscopic thrombi formation (and related severe thrombosis), and focus instead on microthrombi formation. In this context, it is interesting to note that, even if a slight shift in blood coagulation towards a pro-thrombotic state is observed, this may be considered as an indicator of serious damage, produced by an inflammatory or an oncological process.

On the other hand, some simplifications were made when modeling a tissue pathological process. In particular, it was supposed that the primary activator spreads in a traveling-wave manner, which implies a linear velocity of the radius growth. This assumption seems to be valid for some early-stage tumors; see, for instance, [53]. However, large malignancies may diminish their growth velocity at later stages. As a matter of fact, there are many models of inflammation and tumor growth to be found in the literature [76–78], and the possibility of incorporating such approaches in our model deserves, in our opinion, to be explored.

Concerning the sensitivity of our results, a few observations are in order. Our numerical experiments with different sets of parameters have shown that, for a wide range thereof, the character of the $L(R)$-curves is similar. In particular, if activation of blood coagulation is weak, the microthrombi cloud is observed only if the value of $M_{\rm cr}$ is taken to be rather small. If activation is strong, a cloud can be observed, even for comparatively large values of $M_{\rm cr}$. Related to this, it was shown in Sect. 3 that the microthrombi size that can be observed by US device depends upon the selected wavelength λ; see (3.6). This means that microthrombi may be observed by US devices, even in low-polymerized suspensions. Actually, modern US instruments have high sensitivity: they can detect up to a 10^{-11} part of emitted energy [46, Chap. 10]. This provides a unique chance to detect very early stages of early microthrombi appearance in vessels; one merely has to tune the frequency in a suitable manner [16]. A similar remark applies to our model: a microthrombi cloud may be observed, even if blood coagulation activation is weak. One just needs to select a sufficiently small value of $M_{\rm cr}$.

The problem of attenuating tissue processes, when radii change as, for instance, in Fig. 4b for $R_i < R_{\rm cr}$ is also of some interest. Since a smaller radius means less activation of blood coagulation, the cloud should then shrink and L should grow. This suggests a possible way to detect a pulsating tissue pathological process. For instance if in a recovering organism L increases first and then decreases, a periodic activity of tissue pathological source might be considered as an hypothesis.

Overcoming some of the limitations sketched above, and exploring some of the possible research directions sketched, leads to considerable mathematical difficulties. We intend to address such issues in future work.

Acknowledgements The authors express their thanks to the company Spectromed (Moscow), Russian Foundation of Basic Research (Grant 07-04-01523-a), International Science and Technology Center (Grant No. 3744), Universidad Complutense de Madrid and to Spanish Research Grant MICINN 2008-01867 for their support. We also thank S. Uzlova, K. Guria for interesting discussions during the preparation of this manuscript and A.I. Vorob'ev for support of the work.

References

1. Goethe JW (1906) Faust, Part 1 (trans: Swanwick A). George Routledge & Sons, London
2. McFarlane RG (1966) The basis of the cascade hypothesis of blood clotting. Thromb Diath Haemorrh 15:591–602
3. Davie EW (1995) Biochemical and molecular aspects of the coagulation cascade. Thromb Haemost 74(1):135–153
4. Hockin MF, Jones KC, Everse SJ et al (2002) A model for the stoichiometric regulation of blood coagulation. J Biol Chem 277:18322–18333
5. Beltrami E, Jesty J (1995) Mathematical analysis of activation thresholds in enzyme-catalyzed positive feedbacks: application to the feedbacks of blood coagulation. PNAS 92(19):8744–8748
6. Ataullakhanov FI, Guria GT (1994) Spatial aspects of human blood clotting dynamics I. Hypothesis. Biophysics 39:89–96
7. Ataullakhanov FI, Guria GT, Safroshkina AYu (1994) Spatial aspects human blood clotting dynamics II. Phenomenological model. Biophysics 39:979–1068
8. Ataullakhanov FI, Guria GT, Sarbash VI et al (1998) Spatiotemporal dynamics of clotting and pattern formation in human blood. Biochim Biophys Acta 1425:453–468
9. Tyurin KV, Khanin MA (2006) Hemostasis as an optimal system. Math Biosci 204:167–184
10. Wagenvoord R, Hemker PW, Hemker HC (2006) The limits of simulation of the clotting system. J Thromb Haemost 4:1331–1338
11. Guy RD, Fogelson AL, Keener JP (2007) Fibrin gel formation in a shear flow. Math Med Biol 24:111–130
12. Guria GTh, Herrero MA, Zlobina KE (2009) A mathematical model of blood coagulation induced by activation sources. Discr Cont Dyn Syst A 25(1):175–194
13. Mikell FL, Asinger RW, Elsperger KJ et al (1982) Regional stasis of blood in the dysfunctional left ventricle: echocardiographic detection and differentiation from early thrombosis. Circulation 66(4):755–763
14. Uzlova SG, Guria KG, Shevelev AA et al (2008) Acustically detected intravascular micro-clots as predictors of thrombotic postoperative complications (Russian). In: Bulletin of A.N. Bakilev's National Centre for Cardiovascular Surgery NCSSH, Cardiovascular diseases, vol 5, pp 55–64
15. Huang CC, Wang SH, Tsui PH (2005) Detection of blood coagulation and clot formation using quantitative ultrasonic parameters. Ultrasound Med Biol 31(11):1567–1573
16. Uzlova S, Guria K, Guria GTh (2008) Acoustic determination of early stages of intravascular blood coagulation. Philos Trans R Soc A 366:3649–3661
17. Daniel WG, Nellessen U, Schroder E, Nonnast-Daniel B, Bednarski P, Nikutta P, Lichtlen PR (1988) Left atrial spontaneous echo contrast in mitral valve disease: an indicator for an increased thromboembolic risk. J Am Coll Cardiol 11(6):1204–1211
18. Zlobina KE, Guria GTh (2006) Acoustically detected intravascular microaggregation phenomenon caused by pathological processes in tissue. Mathematical model. Similarity laws (Russian). Thromb Hemost Rheol 2:3–14
19. De Cicco M (2004) The prothrombotic state in cancer: pathogenic mechanisms. Crit Rev Oncol Hematol 50:187–196
20. Levi M, van der Poll T, Büller HR (2004) Bidirectional relation between inflammation and coagulation. Circulation 109:2698–2704
21. Esmon CT (2004) Interactions between the innate immune and blood coagulation systems. Trends Immunol 25(10):536–542
22. Levi M (2009) Disseminated intravascular coagulation in cancer patients. Best Pract Res Clin Haematol 22(1):129–136
23. Kumar R, Gupta V (2008) Disseminated intravascular coagulation: current concepts. Indian J Pediatr 75(7):733–738
24. Schmeltzer JWP (2008) Nucleation theory and applications. Dubna, JINR
25. Jones KC, Mann KG (1994) A model for tissue factor pathway to thrombin. J Biol Chem 269(37):23367–23373
26. Qiao YH, Liu LJ, Zeng YJ (2005) A kinetic model for simulation of blood coagulation and inhibition in the intrinsic path. J Med Eng Technol 29(2):70–74
27. Zhu D (2007) Mathematical modeling of blood coagulation cascade: kinetics of intrinsic and extrinsic pathways in normal and deficient conditions. Blood Coagul Fibrinolysis 18(7):637–646
28. Turing AM (1952) The chemical basis of morphogenesis. Philos Trans R Soc Lond B Biol Sci 237(641):37–72
29. Gierer A, Meinhardt H (1972) A theory of biological pattern formation. Kybenetik 12:30–39
30. Meinhardt H (1982) Models of biological pattern formation. Academic Press, London
31. Murray JD (2003) Mathematical biology II. Springer, New York
32. Fisher RA (1937) The wave of advance of advantageous genes. Ann Eugen 7:353–369
33. Kolmogorov AN, Petrovskii IG, Piskunov NS (1937) Study of the diffusion equation with growth of the quantity of matter and its application to a biology problem. In: Bulletin de l'universite d'Etat a Moscou, Serie internationale, Section A 1, pp 1–25 (translation from French to English in: Pelce P (ed) (1988) Dynamics of curved fronts. Academic Press, Boston)
34. Mikhailov AS (1994) Foundations of synergetics I. Distributed active systems, 2nd edn. Springer, Berlin
35. Ataullakhanov FI, Zarnitsyna VI, Kondratovich AYu, Sarbash VI (1997) A new class of stopping self-sustained waves: a factor determining the spatial dynamics of blood coagulation. Physics-Uspekhi (Adv Phys Sci) 172(6):671–690

36. Smoluchowski M (1917) Versuch einer mathematischen Theorie der Koagulationskinetik kolloider Lösungen. Z Phys Chem 92:124–168
37. Chandrasekhar S (1943) Stochastic problems in physics and astronomy. Rev Mod Phys 1:1–91
38. Friedlander SK (2000) Smoke, dust and haze: fundamentals of aerosol dynamics. Oxford University Press, New York
39. Stockmayer WH (1943) Theory of molecular size distribution and gel formation in branched-chain polymers. J Chem Phys 11(2):45–55
40. Leyvraz F, Tschudi HR (1981) Singularities in the kinetics of coagulation processes. J Phys A 14:3389–3405
41. Herrero MA, Rodrigo MR (2007) Remarks on accessible steady status for some coagulation-fragmentation systems. Discr Cont Dyn Syst A 17:541–552
42. Wiltzius P, Dietler G, Kanzing W et al (1982) Fibrin aggregation before sol–gel transition. Biophys J 38:123–132
43. Flory PJ (1941) Molecular size distribution in three dimensional polymers. I. Gelation. J Am Chem Soc 63:3038–3090
44. van Dongen P, Ernst MH (1984) Kinetics of reversible polymerization. J Stat Phys 37:301–329
45. Shaw SM, Kimmey MB (2000) General principles of endoscopic ultrasonographic imaging. Tech Gastrointest Endosc 2(2):50–55
46. Hill CR, Bamber JC, ter Haar GR (eds) (2004) Physical principles of Medical ultrasonics. Wiley, Chichester
47. Volkenstein MV (1977) Molecular biophysics. Academic press, New York
48. Sandkühler P, Sefcik J, Morbidelli M (2004) Kinetics of gel formation in dilute dispersions with strong attarctive particle interactions. Adv Colloid Interface Sci 108(109):133–143
49. Rickles FR, Falanga A (2001) Molecular basis for the relationship between thrombosis and cancer. Thromb Res 102:V215–V224
50. Zwaal RFA, Hemker HC (eds) (1986) Blood coagulation. Elsevier, Amsterdam
51. FitzHugh R (1955) Mathematical models of threshold phenomena in the nerve membrane. Bull Math Biophys 17:257–278
52. Keener J, Sneyd J (1998) Mathematical physiology. Springer, New York
53. Kolobov AV, Gubernov VV, Polezhaev AA (2009) Autowaves in a model of growth of an invasive tumor. Biofizika 54(2):334–342
54. Zel'dovich YaB, Frank-Kamenenetzki DA (1938) A theory of thermal propagation of flame. Acta Physicochim U.S.S.R IX(2):341–350 (in Russian) (English translation in Pelce P (ed) (1988) Dynamics of curved fronts. Academic Press, Boston)
55. Fife PC, Mc Leod JB (1977) The approach of solutions of nonlinear diffusion equations to travelling front solutions. Arch Ration Mech Anal 65:335–361
56. Fife PC, Mc Leod JB (1981) A phase plane discussion of convergence to travelling fronts for nonlinear diffusion. Arch Ration Mech Anal 75:281–314
57. Belintsev BN, Dibrov BF, Livshits MA et al (1978) Nonlinear stability in distributed trigger system. Biological barrier. Biofizika (Russian) 23(5):864–869
58. Lobanov AI, Starozhilova TK, Guria GT (1997) Numerical investigation of pattern formation in blood coagulation. Matematichaskoe Modelirovanie (Russian) 9(8):83–95
59. Barenblatt GI (1996) Scaling, self-similarity, and intermediate asymptotics. Cambridge University Press, New York
60. Liggett JM (1994) Fluid mechanics. McGraw Hill, New York
61. Anderson JD Jr (1995) Computational fluid dynamics: the basics with applications. McGraw-Hill, New York
62. Hagen CHL (1839) Uber die Bewegung des Wassers in engen cylindrischen Rohren. Ann Phys Chem 42:423–442
63. Poiseuille J (1840) Recherches experimentelles sur le mouvement des liquids dans les tubes de tres petits diametres. Comptes Rendus 11:961–1041
64. Schmidt RF, Tews G (eds) (1989) Human physiology, 2nd edn. Springer, Berlin
65. DeBakey ME (1997) New living heart. Adams, Holbrook
66. Guyton AC, Hall JE (2000) Textbook of medical physiology. WB Saunders, Philadelphia
67. Ataullakhanov FI, Volkova RI, Guriya GT, Sarbash VI (1995) Spatial aspects of the dynamics of blood coagulation. III. Thrombus growth in vitro. Biophysics 40:1320–1328
68. Kastrup CJ, Runyon MK, Shen F, Ismagilov RF (2006) Modular chemical mechanism predicts spatiotemporal dynamics of initiation in the complex network of hemostasis. PNAS 103(43):15747–15752
69. Brown EB, Boucher Y, Nasser S, Jain RK. (2004) Measurement of macromolecular diffusion coefficients in human tumors. Microvasc Res 68(3):313–314
70. Ramanujan S, Pluen A, McKee TD, Brown EB, Boucher Y, Jain RK (2002) Diffusion and convection in collagen gels: implications for transport in the tumor interstitium. Biophys J 83(3):1650–1660
71. Lewis SD, Shields PP, Shafer JA (1985) Characterization of the kinetic pathway for liberation of fibrinopeptides during assembly of fibrin. J Biol Chem 260(18):10192–10199
72. Weisel JW, Veklich Y, Gorkun O (1993) The sequence of cleavage of fibrinopeptides from fibrinogen is important for protofibril formation and enhancement of lateral aggregation. J Mol Biol 232:285–297
73. Hantgan RR, Hermans J (1979) Assembly of fibrin. A light scattering study. J Biol Chem 254(22):11272–11281
74. Bru A, Albertos S, Subiza JL et al (2003) The universal dynamics of tumor growth. Biophys J 85(5):2948–2961
75. Oran ES, Boris JB (1987) Numerical simulation of reactive flow. Elsevier Science, New York
76. Sherratt JA, Chaplain MAJ (2001) A new mathematical model for avascular tumour growth. J Math Biol 43:291–312
77. Reynolds A, Rubin J, Clermont G et al (2006) A reduced mathematical model of the acute inflammatory response: I. Derivation of model and analysis of anti-inflammation. J Theor Biol 242(1):220–236
78. Astanin S, Tosin A (2007) Mathematical model of tumour cord growth along the source of nutrient. Math Model Nat Phenom 2(3):153–177